The Ba(Bi$_{0.5}$Ta$_{0.5}$)O$_3$ modified (K$_{0.5}$Na$_{0.5}$)NbO$_3$ lead-free transparent ferroelectric ceramics with high transmittance and excellent energy storage performance

Huangtao Wu[1], Shaoyang Shi[1], Xiang Liu[1], Hua Wang[1,2,*] , Jiwen Xu[1,2], Ling Yang[1], Wei Qiu[1], and Shangju Zhou[1]

[1] School of Materials Science and Engineering, Guilin University of Electronic Technology, Guilin 541004, People's Republic of China
[2] Guangxi Key Laboratory of Information Materials, Guilin University of Electronic Technology, Guilin 541004, People's Republic of China

ABSTRACT

For solving the contradiction that good optical properties and electrical properties of (K$_{0.5}$Na$_{0.5}$)NbO$_3$ (KNN)-based transparent ferroelectric ceramics cannot be achieved at the same time. The modification by doping and improved sintering techniques can not only increase the optical properties of ceramics but also improve and enhance the electrical properties of ceramics. $(1 - x)$(K$_{0.5}$Na$_{0.5}$)NbO$_3$–xBa(Bi$_{0.5}$Ta$_{0.5}$)O$_3$ (x = 0.01, 0.015, 0.02, 0.025, 0.03) lead-free transparent ferroelectric ceramics were synthesized by conventional solid-phase sintering method. The KNN ceramic was modified by Ba(Bi$_{0.5}$Ta$_{0.5}$)O$_3$ to obtain a large optical band gap energy, submicron grains, and a highly symmetric phase structure when x = 0.025, thus gaining highly transmittance of 67.2% in near-infrared region. The smaller grain size and dense microstructure give the ceramic with x = 0.025 a higher dielectric breakdown strength. Therefore, the excellent energy storage performance is achieved at high electric field of 200 kV/cm with energy storage density (W_{rec}) and energy storage efficiency (η) of 1.41 J/cm^3 and 42%, respectively. The results show that (K$_{0.5}$Na$_{0.5}$)NbO$_3$–Ba(Bi$_{0.5}$Ta$_{0.5}$)O$_3$ ceramics are considered to be excellent candidates for the field of new transparent electronic devices.

Ⓐ Springer

1 Introduction

In recent decades, electronic information technology welcomed the golden period of development, spurring rapid development in the field of electronic devices like military communications, medical devices, mobile devices, LCD screens, etc. [1–4]. Transparent ferroelectric ceramics are a type of optoelectronic ceramic with good optical and electrical properties, which are widely used in the fields of transparent pulse capacitors, sensors, storage, and transparent electronic components [5–7]. Among them, lead zirconate titanate (PZT) and La-doped lead zirconate titanate (PLZT) transparent ferroelectric ceramics are widely used to apply transparent ferroelectric ceramics, which have high piezoelectric constants, electromechanical coupling coefficients and superior optoelectronic performance [8–11]. However, with the massive development and application of lead (Pb) containing ceramics and the gradual rise of people's environmental awareness. Although PZT and PLZT ceramics are sought after for their excellent optoelectronic properties. High Pb content not only pollutes the environment but also causes irreversible damage and harm to the body in people's long-term daily use [12, 13]. Therefore, it is imperative to find alternative lead-free ceramics.

KNN ferroelectric ceramics possess high Curie temperatures, piezoelectric coefficients, electromechanical coupling coefficients, and good optoelectronic properties which make them considered excellent candidates for PZT and PLZT ceramics [6, 14, 15]. However, the pure KNN ferroelectric ceramics are usually low transparent, which is related to many factors such as the optical band gap energy, grain size, refraction, birefringence and crystal structure, etc. [16–18], which has been confirmed by many research scholars. Some studies have shown that larger optical band gap energy and smaller grain size are beneficial to obtaining higher transmittance [19]. In addition, the crystal structure has a crucial influence on the light transmission in KNN ceramics [20]. KNN ferroelectric ceramics exhibit a typical orthorhombic phase at room temperature with the low symmetry of the crystal structure, resulting in reduced transmittance [20–23]. Numerous studies have shown that doping modifications and improved sintering techniques can not only enhance the light transmission in KNN ceramics

but also significantly improve its comprehensive electrical properties [24–29].

Currently, doping modifications are generally based on the addition of oxides (Al_2O_3, La_2O_3, Y_2O_3, etc.) and similarly structured second components (perovskite structure, ABO_3) to KNN ceramic substrates [5, 30, 31], and sintering techniques used to improve properties of KNN ceramics are usually conventional solid-phase sintering method, hot-press sintering method, special atmosphere sintering method, plasma sintering method, etc. [28, 32]. Zhao et al. prepared KNN–$Sr(Al_{0.5}Nb_{0.5})O_3$ transparent ferroelectric ceramics with submicron grains by pressureless sintering method to obtain good transmittance of 55% at 780 nm, and excellent electrical properties such as piezoelectric constants (d_{33} = 105 pC/N), dielectric constant (ε_r = 1021), and residual polarization (P_r = 15.1 μC/cm^2) [33]. Geng et al. prepared $[(K_{0.5}Na_{0.5})_{1-2x}(Sr_{0.75}Ba_{0.25})_x]_{0.93}Li_{0.07}Nb_{0.93}Bi_{0.07}O_3$ lead-free transparent ferroelectric ceramics by hot-press sintering method, obtaining a high transmittance of 60% in the visible band and even close to 100% transparency in the infrared band, while combining excellent electrical properties (ε_r = 1679 and d_{33} = 151 pC/N) [34]. Therefore, the improvement and enhancement of the optoelectronic properties for KNN ceramics through doping modification and improved sintering techniques would be more convenient, feasible, effective, and low-cost.

As introduced before, electronic information and internet technology is advancing. Therefore, the requirements for KNN-based transparent ferroelectric ceramics are constantly being updated. Nowadays, the multi-functional and high-performance KNN-based transparent ferroelectric ceramics are better suited to the requirements of connectivity, diversity, and high standards among a wide range of transparent electronic devices. In this work, ($K_{0.5}Na_{0.5}$)NbO_3–$Ba(Bi_{0.5}Ta_{0.5})O_3$ transparent ferroelectric ceramics were synthesized using a low-cost and easily prepared conventional solid-phase sintering method. The expectation is to obtain high-performance and multi-functional ceramics by the addition of $Ba(Bi_{0.5}Ta_{0.5})O_3$. The phase structure transition, microscopic morphology changes, and optoelectronic properties of the ceramics were investigated in detail. Further analysis of the contribution from the optical band gap to the transmittance in ceramics, and an evaluation of the potential for the ceramics as novel lead-free electronic devices.

2 Experimental procedure

$(1 − x)(K_{0.5}Na_{0.5})NbO_3–xBa(Bi_{0.5}Ta_{0.5})O_3$ lead-free transparent ferroelectric ceramics (abbreviations as KNN–xBBT, x = 0.01, 0.015, 0.02, 0.025, 0.03) were attained by the conventional solid-phase sintering method, in which the raw materials all adopted the high-purity powders and it contained Bi_2O_3 (99.999%), Na_2CO_3 (99.8%), Nb_2O_5 (99.99%), K_2CO_3 (99%), $BaCO_3$ (99.9%), and Ta_2O_5 (99.99%). The raw materials were dried in an oven at 80 °C for 12 h before using, and then calculated and weighed according to different x. The weighed raw materials were put into the ball mill tank and ball milled for 24 h using zirconia balls and ethanol as the medium with the slurry dried at 80 °C after ball milling. Then, the dried powder was calcined at 860 °C for 3 h and ball-milled again for 12 h. The obtained slurry was also dried at 80 °C. The powders were blended with the suitable amount of 7 wt% polyvinyl alcohol (PVA) binder solution and the next passed through 100-mesh screen. Subsequently, under the 5 MPa pressure, they were pressed into circular ceramic sheets with the diameter 13 mm and thickness with 1 mm. Finally, the ceramic sheets were calcined at 600 °C for 2 h to eliminate the PVA added during the granulation process. Immediately afterwards, the sintering was carried out at an increase in temperature of 2 °C/min to 1180 °C for 3 h to densify the ceramic sheets. For all ceramic pieces, the surface was polished smooth and the thickness was approximately 0.3 mm to measure their optical properties. Meanwhile, the ceramic sheets were brushed with silver paste on both sides and calcined at 600 °C for 30 min to test their electrical properties.

Optical transmittance was measured by ultraviolet–visible (UV–Vis, PerkinElmer Lambda 365) spectrophotometer. The crystalline phase structure of the ceramics was investigated through X-ray diffraction (XRD, D8-Advance). The valence of Bi ions was tested using X-ray photoelectron spectroscopy (XPS, Escalab250 Xi). A field emission scanning electron microscope (FE-SEM, Quanta 450 FEG) was utilized to observe the surface morphology of the ceramics, and grain size was calculated and analyzed with the software Nano Measurer 1.2. The polarization–electric field (P–E) hysteresis loops were tested using ferroelectric integrated test system (TZ-FE-C).

3 Results and discussion

Figure 1a shows a XRD diffraction pattern of KNN–xBBT ceramics. From Fig. 1a, it can be seen that all ceramics show a typical perovskite structure [35, 36]. Moreover, no significant second phase is found in all XRD diffraction patterns, which indicates that Ba, Bi and Ta have been diffused into KNN structure. The phase structure of KNN-based transparent ferroelectric ceramics can be roughly determined by the (200) diffraction peaks at $2\theta = 45°$ [37]. Figure 1b reveals that magnified XRD diffraction pattern in the 2θ range of 44°–47°, and Gaussian fitting for the diffraction peak at x = 0.01. It can be clearly found that when x > 0.01, there is only a sharp diffraction peak, indicating that the phase structure of the ceramic is close to a cubic phase. The phase structure at this time can be called a pseudo-cubic phase. However, when x = 0.01, the band at 45° corresponding to (200) symmetry plane has been fitted by software analysis observing be formed by two diffraction peaks associated to (202) and (020) symmetry planes. Meanwhile, the diffraction intensity of the (202) peak is approximately twice higher than with the (020) peak, indicating the ceramic has an orthogonal phase structure resembling pure KNN [36].

In addition, the (200) diffraction peak shifts to the right after the addition of $Ba(Bi_{0.5}Ta_{0.5})O_3$ to the KNN ceramics, which indicates a smaller cell size. This is because Ba^{2+} (R = 1.61 Å, CN = 12) and Bi^{3+} (R = 1.38 Å, CN = 12) preferentially replace K^+ (R = 1.64 Å, CN = 12) and Na^+ (R = 1.39 Å, CN = 12) of similar radius at the A-position, while Ta^{5+} (R = 0.64 Å, CN = 6) replaces Nb^{5+} (R = 0.64 Å, CN = 6) of similar radius at the B-position. This process causes lattice distortion, thus leading to a smaller cell volume and a shift of the (200) diffraction peak to a higher angle [22]. Interestingly, the (200) diffraction peaks are observed to be weakly shifted to lower angles at x > 0.02. This can be attributed to the fact that Bi ions have complex valence states, such as Bi^{3+} and Bi^{5+} [24, 32]. When the $Ba(Bi_{0.5}Ta_{0.5})O_3$ content is low, only Bi^{3+} is present, while with the continuous addition of $Ba(Bi_{0.5}Ta_{0.5})O_3$, a small amount for Bi^{5+} appears. The radius of Bi^{5+} (R = 0.76 Å, CN = 6) is similar to Nb^{5+} (R = 0.64 Å, CN = 6) and will preferentially replace Nb^{5+} at the B-position, resulting in larger cells, and the (200) diffraction peaks shifting to lower angles. To investigate the change in the valence state of the Bi ion

Fig. 1 a XRD diffraction pattern of KNN–xBBT ceramics and b magnified XRD diffraction pattern in the 2θ range of 44°–47°
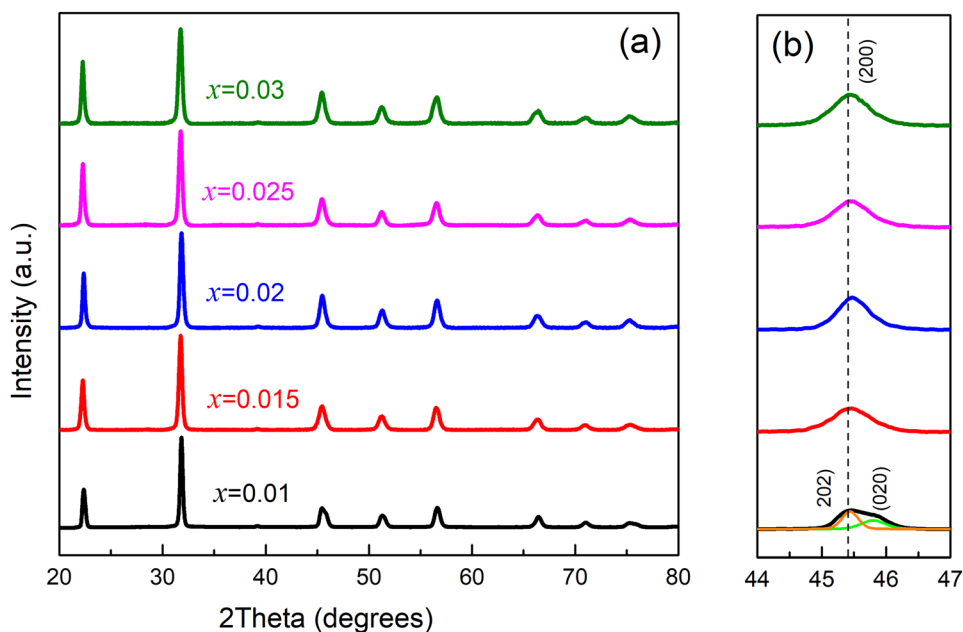
during this process of adding $Ba(Bi_{0.5}Ta_{0.5})O_3$, the XPS spectra of Bi 4f for KNN–xBBT (x = 0.02, 0.025) ceramics were tested and the results are shown in Fig. 2a, b. For x = 0.02, the raw, sum, and Bi^{3+} curves almost overlap and only Bi^{3+} centered at 158.95 eV and 164.26 eV exists. However, from x = 0.02 to 0.025, the Bi 4f broad peak decomposes into two narrow peaks centered at 157.96 eV, 163.32 eV and 158.42 eV, 163.76 eV, corresponding to Bi^{5+} and Bi^{3+}, respectively [38, 39]. In addition, Bi^{3+} is observed to exhibit considerably larger peak areas than that of Bi^{5+}. The results indicate that only Bi^{3+} is present at lower $Ba(Bi_{0.5}Ta_{0.5})O_3$ contents and with the addition

of $Ba(Bi_{0.5}Ta_{0.5})O_3$, a minor amounts of Bi^{5+} appear at x = 0.025.

Table 1 gives the lattice parameters (including a, b, c, V, and c/a) of KNN–xBBT ceramics, which were calculated using jade 6.5 software. With the increase of $Ba(Bi_{0.5}Ta_{0.5})O_3$ content, the ratio of c/a is always approaching to 1, which indicates that the phase structures of the ceramics are all pseudo-cubic phases. At the same time, the ratio of c/a decreases and then increases, reaching a minimum value of 1.0012 at x = 0.025, which indicates that the structural symmetry of KNN–0.025BBT ceramic is higher. Notably, the ratio of c/a is much larger than 1.0012
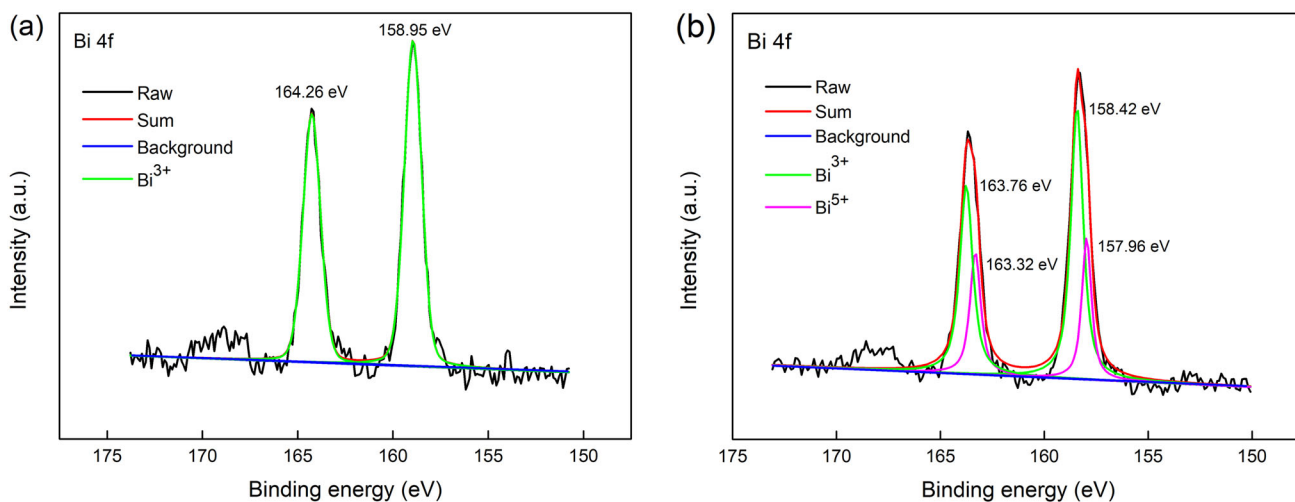

Fig. 2 XPS spectra of Bi 4f for KNN–xBBT ceramics: a x = 0.02 and b x = 0.025

Table 1 Lattice parameters of KNN–xBBT ceramics

x	a (Å)	b (Å)	c (Å)	V (Å^3)	c/a
0.01	3.9868	3.9877	4.0056	63.68	1.0047
0.015	3.9817	3.9859	3.9906	63.33	1.0022
0.02	3.9820	3.9799	3.9897	63.23	1.0019
0.025	3.9850	3.9866	3.9896	63.38	1.0012
0.03	3.9826	3.9922	3.9885	63.41	1.0015

when $x = 0.01$, indicating that the structural symmetry of KNN–0.01BBT ceramic is very poor. In addition, with the increase of Ba(Bi$_{0.5}$Ta$_{0.5}$)O$_3$ content, the cell volume shows a trend of decreasing and then increasing, which coincides with the drift direction of the (200) diffraction peak analyzed in the previous section.

Figure 3a shows a photograph of KNN–xBBT transparent ceramics. From Fig. 3a, it can be seen that all ceramic samples show a high transparency, while the words underneath the ceramic samples can be also clearly observed. Figure 3b displays an example picture of KNN–0.025BBT transparent ceramics. The "Caution Ventilation" sign behind the ceramic sample can be clearly seen in Fig. 3b, which indicates that the ceramic has good potential for applications in the visible range. To better analysis the variation of transmittance, the transmittance spectra and transmittance as a function of content (x) for KNN–xBBT

Fig. 3 a Photograph of KNN–xBBT transparent ceramics and **b** example picture of KNN–0.025BBT transparent ceramic

transparent ceramics are shown Fig. 4a and b, respectively. As can be seen in Fig. 4a, when the wavelength is greater than 400 nm, the transmittance begins to grow rapidly with increasing wavelength, reaching a maximum transmittance at 1100 nm. From Fig. 4b, it can be analyzed that both in the visible region (780 nm) and in the near-infrared region (1100 nm), the transmittance of ceramics tends to increase and then decrease with the increase of x, showing an obvious composition dependence. This phenomenon is basically consistent with the photograph shown in Fig. 3a. Interestingly, when $x < 0.025$, the transmittance of ceramics increases significantly with increasing Ba(Bi$_{0.5}$Ta$_{0.5}$)O$_3$ content, and the maximum transmittance is obtained at $x = 0.025$. However, with the continuous addition of Ba(Bi$_{0.5}$Ta$_{0.5}$)O$_3$, the transmittance decreases slightly. This is due to the decrease in structural symmetry for ceramics after the addition of excess Ba(Bi$_{0.5}$Ta$_{0.5}$)O$_3$, which leads to a decrease in light transmittance [15]. Especially, KNN–0.025BBT transparent ceramic has a good transmittance of 52.8% in the visible range (780 nm) and even obtain an extremely high transmittance of 67.2% in the near-infrared region (1100 nm). The ceramic shows great potential for application in the field of lead-free transparent electronic devices.

Further studies have shown that the transmittance of ceramics is close to 0 at wavelengths of 200–400 nm, which is mainly caused by interband jumping and is related to the optical band gap [15, 40]. The interband jump of KNN-based ceramics is a direct jump, which can be calculated by the Tauc formula to obtain the optical band gap energy (E_g) [41, 42], and the calculation equation is as follows:

$$(\alpha h v)^2 = A(h v - E_g), \tag{1}$$

where α is the absorption factor, v is the photon frequency. The h and A are the Planck constant and constant, respectively. Therein, the α can be calculated from the following equation:

$$\alpha = \frac{1}{t} \ln\left(\frac{1}{T}\right), \tag{2}$$

where t is the thickness of the sample and T is the transmittance of the ceramic. The value of E_g can be obtained by extrapolating the tangent line of the $(\alpha h v)^2$–$h v$ curve to 0, and the results are shown in Fig. 5a–e. It can be directly seen that the values of E_g for ceramics are 2.644 eV, 2.686 eV, 2.858 eV,
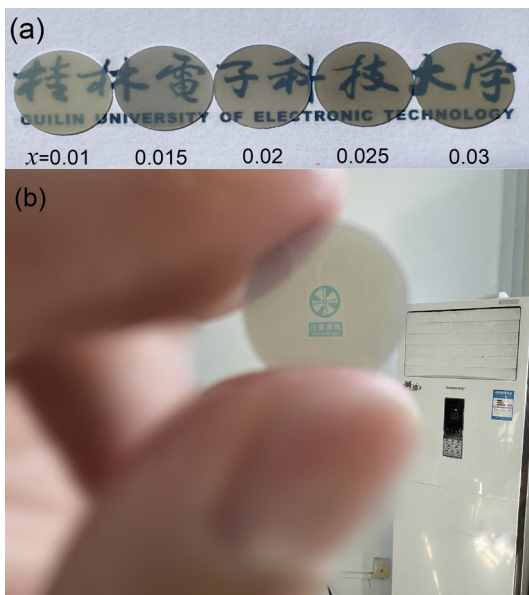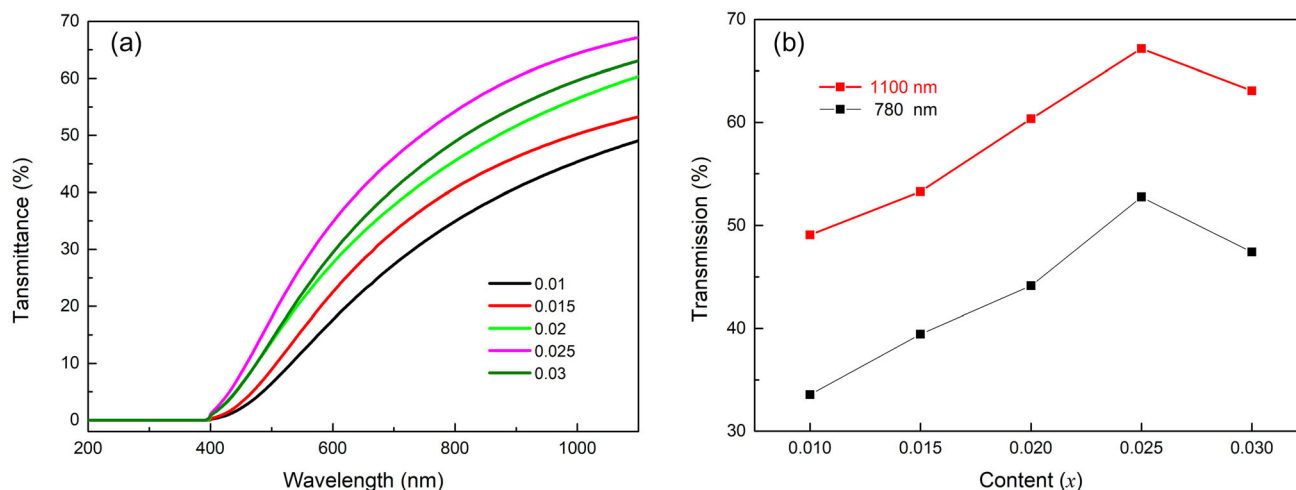
Fig. 4 **a** Transmittance spectra and **b** transmittance as a function of content (x) for KNN–xBBT transparent ceramics

2.929 eV and 2.871 eV when $x = 0.01$, 0.015, 0.02, 0.025, 0.03, respectively. Figure 5f shows the E_g values of KNN–xBBT ceramics. From Fig. 5f, the E_g of the ceramics changes significantly as x increases. Particularly, the value of E_g increases by 0.285 eV for $x = 0.01$ to 0.025, indicating the presence of Ba(Bi$_{0.5}$Ta$_{0.5}$)O$_3$ has an important effect on the energy band jump in KNN-based ceramics. As is well-known, light possesses energy. When light passes through ceramics, the total energy consumption of the incident light is mainly the energy band jump by electrons, the transmission, and scattering process for the light. The larger E_g helps to decrease the energy consumed by the process of electron energy band jumping, thus reducing the energy loss from light [19, 43]. The results show that KNN–0.025BBT ceramic with larger value of E_g (2.929 eV) possesses higher transmittance.

The variation of grain size and grain morphology can be known by observing the surface micromorphology in ceramics. For KNN-based transparent ferroelectric ceramics, the grain size and density of the ceramic have a significant impact on enhancing the transmission [15]. Figure 6a–e show the surface micromorphology of KNN–xBBT ceramics and give the statistical results for the particle size distribution as shown in the insets of Fig. 6a–e. As can be seen in Fig. 6a–e, all KNN–xBBT ceramics possess dense microstructures, small pore diameters, and relatively well-distributed grain sizes. However, compared to KNN–xBBT ($x = 0.015$, 0.02, 0.025, 0.03) ceramics, KNN–0.01BBT ceramic has larger particle, pore diameters, and the distribution of grain size is less

uniform, while the grain morphology shows the coexistence with orthorhombic and tetragonal shapes. This also corroborates the XRD results of KNN–0.01BBT ceramic in Fig. 1b. With the Ba(Bi$_{0.5}$Ta$_{0.5}$)O$_3$ content increases, it can be clearly derived from Fig. 6a–e and their insets that the grain size of the ceramics gradually decreases when $x \leq 0.025$. At the same time, the tightly stacked grains make the pore size and porosity also gradually reduce. As for the anomaly at $x = 0.03$, this is due to the addition of excess Ba(Bi$_{0.5}$Ta$_{0.5}$)O$_3$ changing the lattice parameters, thus leading to a slight increase grain size. When $x = 0.025$, the ceramics possess smaller a grain size and dense microstructure, resulting in a uniform grain size distribution and fewer residual pores. In this case, it is beneficial to reduce light scattering, and leads to more light through the ceramics, which can effectively improve the transmittance of the ceramics. For better analysis of the variation in grain size, the average grain size of KNN–xBBT ceramics is shown Fig. 6f. With increasing content of x, the grain size in ceramics first decreases from 173.95 nm at $x = 0.01$ to 98.48 nm at $x = 0.025$, and then increases slightly to 107.86 nm at $x = 0.03$, indicating small amounts for Ba(Bi$_{0.5}$Ta$_{0.5}$)O$_3$ have the effect of inhibiting grain growth. Remarkably, the scattering coefficient reaches its maximum value when the size of the light scattering center (such as: grain size, aperture, etc.) is approaching the wavelength of incident light (200–1100 nm), whereas refining the grains to submicron level (≤ 1 µm) is the most effective way for reducing the scattering coefficient [33, 44]. Therefore,
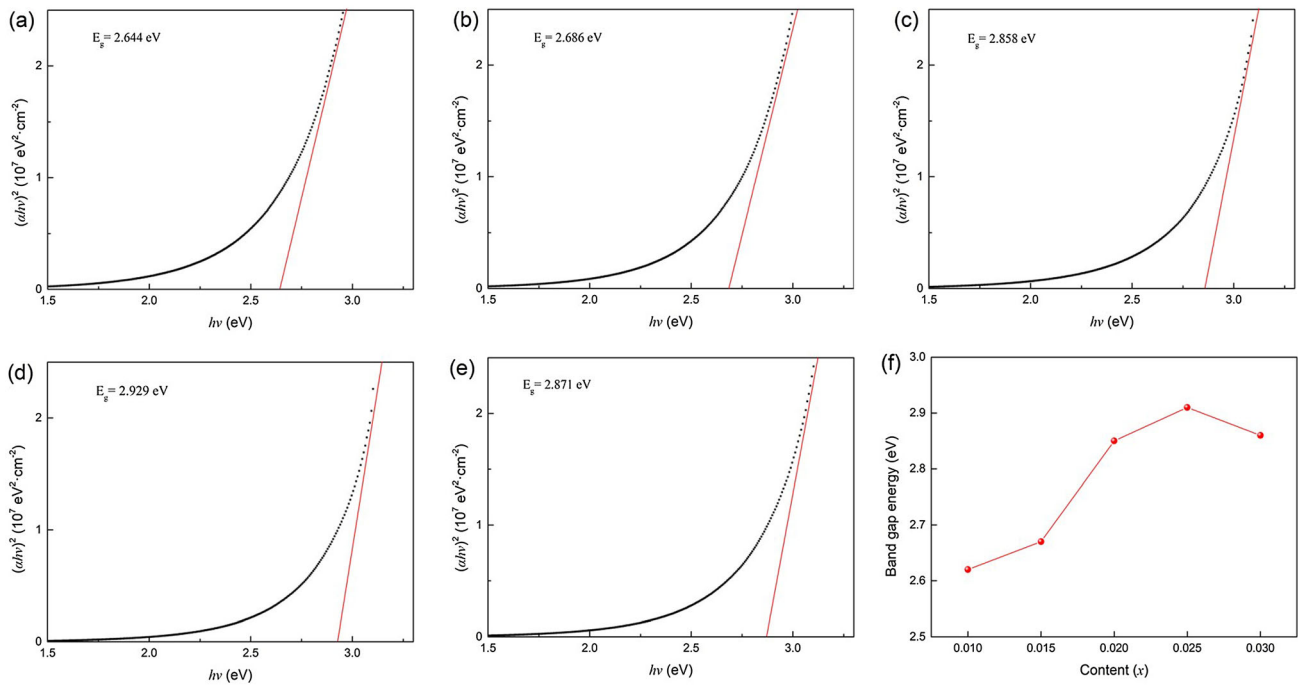
Fig. 5 **a–e** Optical band gap diagrams and **f** E_g values of KNN–xBBT ceramics

KNN–0.025BBT ceramic with smaller grain size ($\sim$ 0.1 µm) possesses higher transmittance.

Figure 7a shows the P–E hysteresis loops of KNN–xBBT ceramics under 140 kV/cm. As can be seen, all KNN–xBBT ceramics exhibit saturated P–E hysteresis loops. With the addition of Ba(Bi$_{0.5}$Ta$_{0.5}$)O$_3$ and the value of P_r begins to decrease, indicating a weakening of ferroelectricity [44]. The elongated P–E loop is a typical feature of relaxed ferroelectrics, which is beneficial for obtaining the higher energy storage characteristics [45]. For better analysis of the energy storage performance, the saturation polarization (P_m), residual polarization (P_r), energy storage density (W_{rec}) and energy storage efficiency (η) of KNN–xBBT ceramics are shown in Fig. 7b. The W_{rec} and η can be calculated from the P–E hysteresis loops according to the equations below [30]:

$$W_{rec} = \int_{P_r}^{P_m} E dP, \tag{3}$$

$$W = \int_{0}^{P_m} E dP, \tag{4}$$

$$\eta = \frac{W_{rec}}{W} \times 100\%, \tag{5}$$

where W is electric energy storage density, E is the electric field, and P is the polarization. As seen from the integral equation, P_m and P_r have an important effect on W_{rec}. From Fig. 7b, it can be seen that P_m and P_r show an overall decreasing trend with increasing x, while W_{rec} also shows decreasing trend in general. However, P_m increases rapidly from 12.58 µC/cm^2 at $x = 0.02$ to 13.98 µC/cm^2 at $x = 0.025$, while P_r increases slightly from 3.31 µC/cm^2 at $x = 0.02$ to 3.60 µC/cm^2 at $x = 0.025$. This change causes the W_{rec} of the ceramics between $x = 0.02$ and 0.03, there is a kind of leap in growth. This is due to the small amount of Bi^{5+} which enhances the optical anisotropy and contributes to improve the electrical properties in ceramics, such as P_m, P_r, W_{rec}, etc. In addition, the η value gradually increases with the addition of Ba(Bi$_{0.5}$Ta$_{0.5}$)O$_3$. The best integrated energy storage performance is reached at $x = 0.025$, at which the W_{rec} and η are 0.61 J/cm^3 and 52%, respectively.

The small grain size and dense microstructure effectively improve the dielectric breakdown strength, DBS [46]. Meanwhile, extremely large P_m is obtained at high electric field, which is favorable to improve the W_{rec} of ceramics. Figure 8a, b show the P–E hysteresis loops of KNN–xBBT ($x = 0.01$, 0.025) ceramics at 140 and 200 kV/cm. At 140 kV/cm, the ceramics exhibit typical ferroelectricity. When the
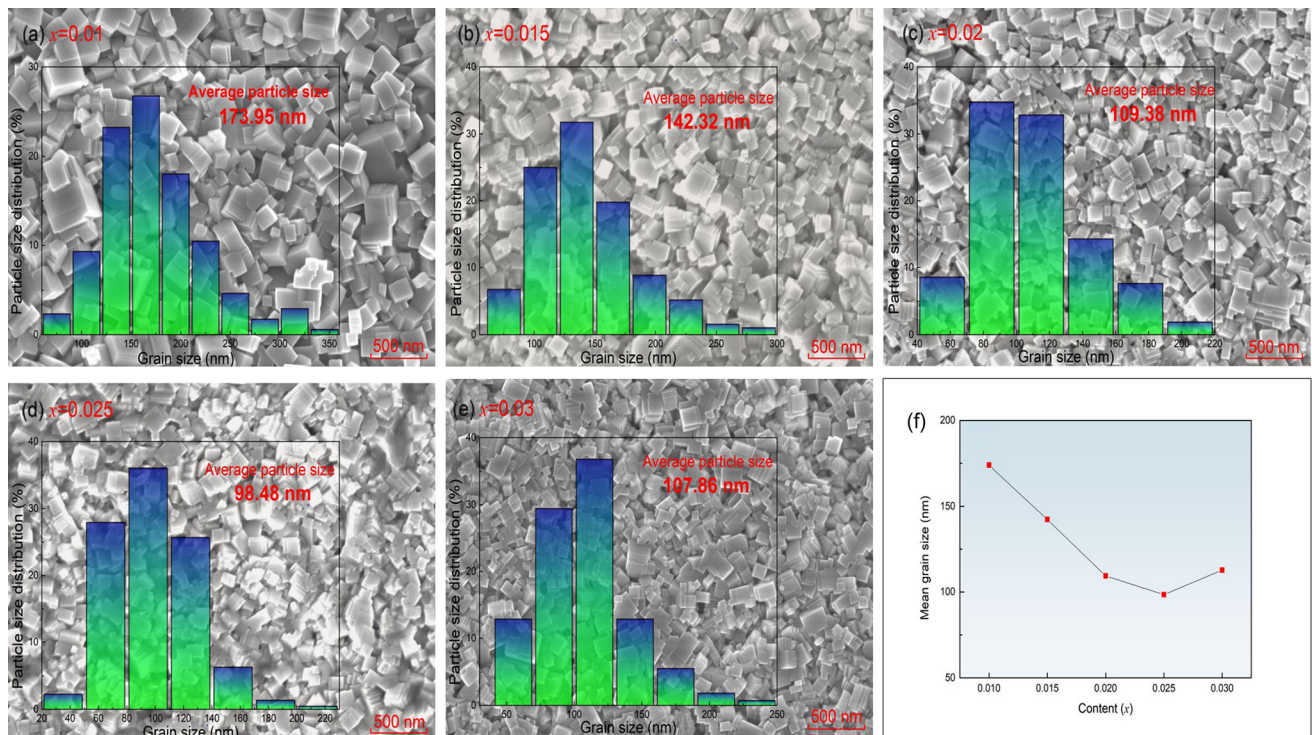
Fig. 6 a–e Surface micromorphology, grain size distribution and **f** average grain size of KNN–xBBT ceramics

electric field is increased to 200 kV/cm, an obvious "swelling" P–E loop appears at x = 0.01, which is caused by increased leakage current and the high residual polarization [47]. However, at x = 0.025, the ceramics possess the values of high DBS due to the small grain size and dense microstructure. Therefore, saturated P–E loops can still be obtained under a large electric field of 200 kV/cm, indicating that the ceramics have good electrical properties. The results show that the DBS value of KNN–0.025BBT ceramic with smaller grain size is significantly higher than that of KNN–0.01BBT ceramic with larger grain size. The DBS values of ceramics with x = 0.01 and 0.025 were tested to be about 200 kV/cm and 230 kV/cm, respectively. Figure 8c shows the W_{rec} and η of KNN–0.025BBT ceramic under different electric fields. As the electric field strength increases, W_{rec} gradually increases from 0.61 J/cm^3 at 140 kV/cm to 1.41 J/cm^3 at 200 kV/cm, while η overall gradually decreases from 52% at 140 kV/cm to 42% at 200 kV/cm. This can be attributed to the extremely high P_m obtained by the ceramic at high electric fields and exacerbates its energy storage loss, leading to W_{rec} increase and η decrease. The results show that KNN–

0.025BBT transparent ferroelectric ceramic not only obtains extremely high transmittance of 67.2% in the near-infrared region (1100 nm), but also combines excellent electrical properties with W_{rec} and η of 1.41 J/cm^3 and 42%, respectively. In fact, KNN–0.025BBT ceramic has a higher energy storage density than the majority of KNN-based transparent ferroelectric ceramics [14, 15, 21, 26, 28, 30, 33, 46], indicating its potential applications in the field of lead-free transparent energy storage electronics like transmission pulse capacitors and memories.

4 Conclusion

$(1 - x)(K_{0.5}Na_{0.5})NbO_3–xBa(Bi_{0.5}Ta_{0.5})O_3$ (x = 0.01, 0.015, 0.02, 0.025, 0.03) lead-free transparent ferroelectric ceramics were prepared by conventional solid-phase sintering method. With the increase of $Ba(Bi_{0.5}Ta_{0.5})O_3$ content, there is a change of phase structure for the ceramics from orthorhombic phase to pseudo-cubic phase. While the grain size gradually decreases in general, reaching a minimum value of 98.48 nm at x = 0.025. Meanwhile, the optical band gap energy E_g reaches a maximum value of 2.929 eV
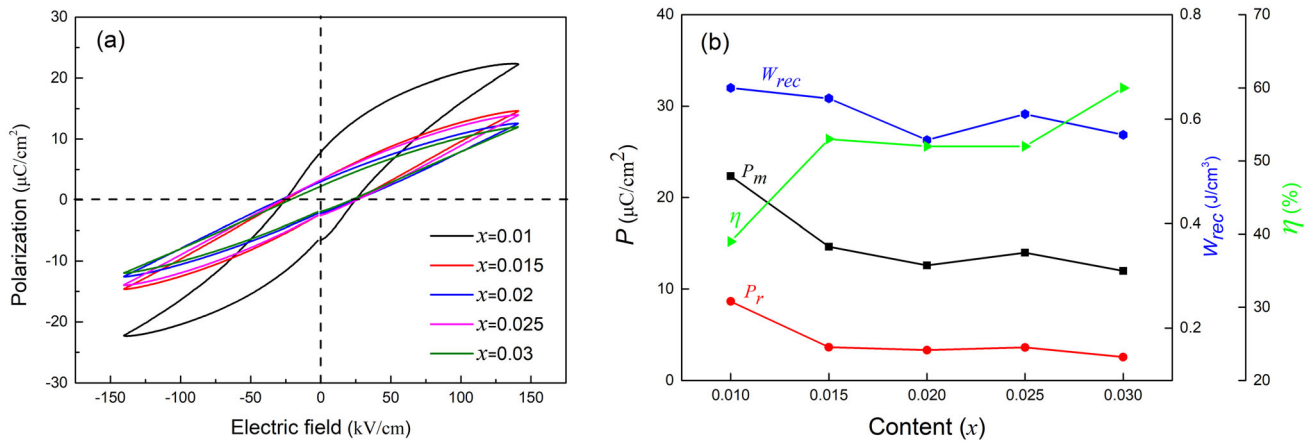
Fig. 7 **a** P–E hysteresis loops and **b** P_m, P_r, W_{rec} and η of KNN–xBBT ceramics under 140 kV/cm electric field
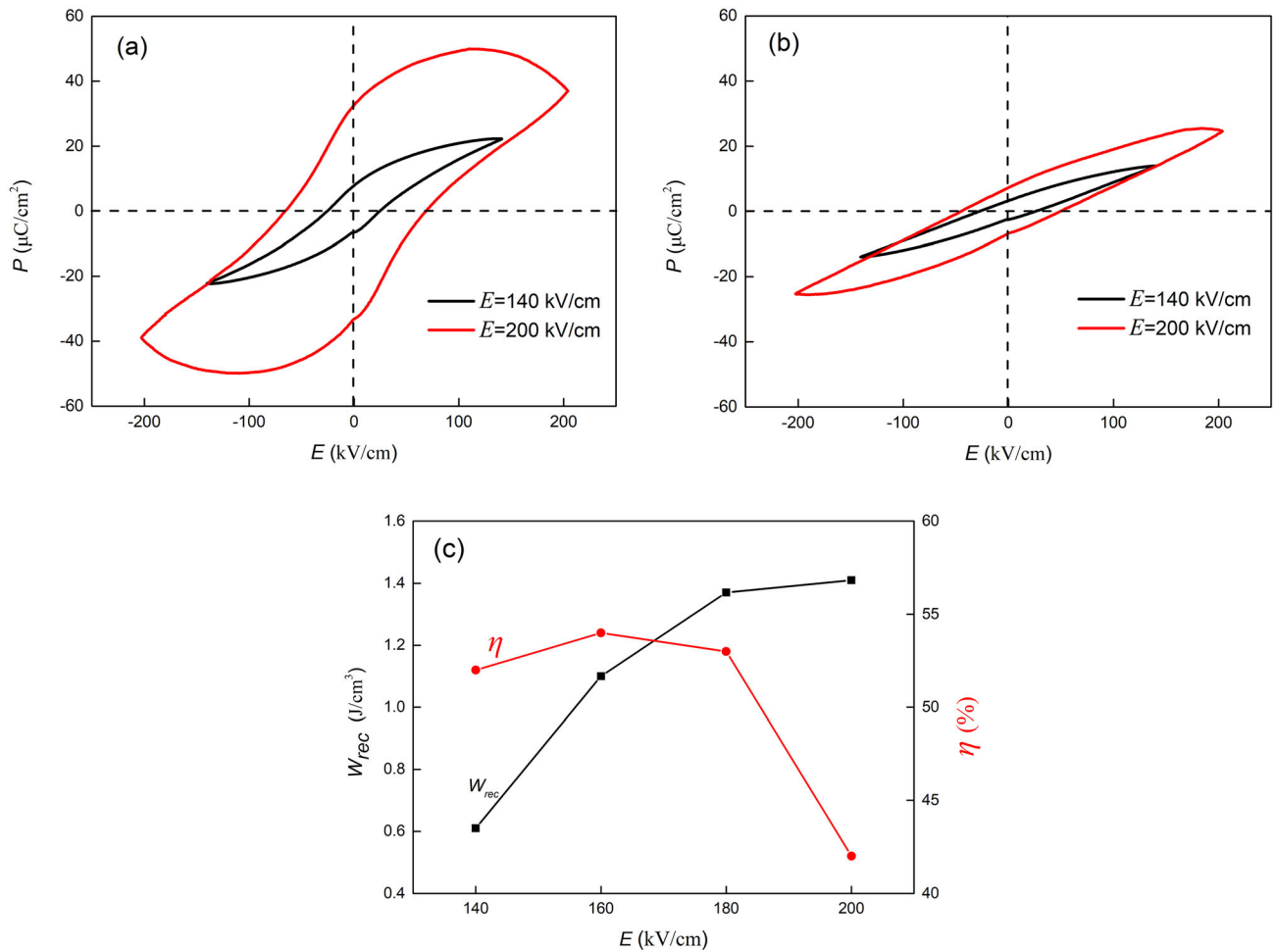

Fig. 8 P–E hysteresis loops of KNN–xBBT ceramics under 140 and 200 kV/cm **a** $x = 0.01$ and **b** $x = 0.025$ and **c** W_{rec} and η of KNN–0.025BBT ceramic under different electric fields

at $x = 0.025$. Further studies have shown that grain size, phase structure, and optical band gap energy have significant effects on the transmittance of

ceramics. At $x = 0.025$, the ceramic has a small grain size, pseudo-cubic phase with high symmetry, and large optical band gap energy which facilitates the

ceramics to obtain excellent optical properties, and gets a very high transmittance of 67.2% in the near-infrared region (1100 nm). Through $Ba(Bi_{0.5}Ta_{0.5})O_3$ doping, the ceramics get good comprehensive electrical properties. The ceramic with smaller grain size and dense microstructure at $x = 0.025$ has higher DBS (DBS ≈ 230 kV/cm). Under the electric field of 200 kV/cm, the high energy storage density ($W_{rec} = 1.41$ J/cm^3) and good energy storage efficiency ($\eta = 42\%$) are obtained, and at this time the ceramic reaches the best comprehensive energy storage performance. The results show that $(K_{0.5}Na_{0.5})NbO_3$–$0.025Ba(Bi_{0.5}Ta_{0.5})O_3$ lead-free transparent ferroelectric ceramics with very high transmittance and excellent electrical properties are a promising and potential candidate for application in the field of lead-free transparent energy storage electronic devices.

Author contributions

All authors jointly participated in the data collection and experimental program exploration. Data collection, analysis and initial manuscript were completed by first author: HW. Revision and refinement of the manuscript was performed by the corresponding author: HW and the manuscript is published with the consent of all authors.

Funding

Date availability

The available in the article are true and valid which are recognized by all authors.

Declarations

Conflict of interest The authors declare no competing financial interest.

References

1. G. Dutta, J. Rainbow, U. Zupancic, S. Papamatthaiou, P. Estrela, D. Moschou, Chemosensors **6**, 43 (2018)

2. J.F. Harvey, M.B. Steer, T.S. Rappaport, IEEE Access **7**, 52350–52359 (2019)

3. H. Cai, J. Lin, Y.J. Lin, Z.J. Liu, H.T. Tang, H.R. Wang, L.G. Zhu, S. Han, ACM Trans. Des. Autom. Electron. Syst. **27**, 1–50 (2022)

4. A. Mansur, T.M. Hauer, M.W. Hussain, M.K. Alatwi, A. Tarazi, M. Khodadadi, C.H. Tator, J. Neurotrauma **35**, 1886–1894 (2018)

5. Z.H. Xiao, S.J. Yu, Y.M. Li, S.C. Ruan, L.B. Kong, Q. Huang, Z.R. Huang, K. Zhou, H.B. Su, Z.J. Yao, W.X. Que, Y. Liu, T.S. Zhang, J. Wang, P. Liu, D.Y. Shen, M. Allix, J. Zhang, D.Y. Tang, Mater. Sci. Eng. R **139**, 100518 (2020)

6. L.Q. Xu, F. Chen, F. Jin, D. Lan, L.L. Qu, K.X. Zhang, Z.X. Zhang, G.Y. Gao, H.L. Huang, T. Li, F.P. Zhang, K. Wang, Z. Zhou, W.B. Wu, Appl. Phys. Lett. **115**(20), 202901 (2019)

7. M. Zhang, H.B. Yang, D. Li, Y. Lin, J. Alloys Compd. **829**, 154565 (2020)

8. A. Presas, Y.Y. Luo, Z.W. Wang, D. Valentin, M. Egusquiza, Sensors **18**(7), 2251 (2018)

9. S.F. Wang, J. Zhang, D.W. Luo, F. Gu, D.Y. Tang, Z.L. Dong, G.E.B. Tan, W.X. Que, T.S. Zhang, S. Li, L.B. Kong, Prog. Solid State Chem. **41**, 20–54 (2013)

10. Y. Chen, X.L. Bao, C.M. Wong, J. Cheng, H.D. Wu, H.Z. Song, X.R. Ji, S.H. Wu, Ceram. Int. **44**, 22725–22730 (2018)

11. Z.W. Xu, X. Zeng, Z.D. Cao, L. Ling, P.S. Qiu, X.Y. He, J. Electroceram. **44**, 215–222 (2020)

12. P.K. Panda, J. Mater. Sci. **44**, 5049–5062 (2009)

13. H. Wang, X. Zhai, J.W. Xu, L. Yang, J. Wuhan Univ. Technol. Mater. Sci. Ed. **34**, 308–311 (2019)

14. H.T. Wu, G.B. Hu, S.Y. Shi, X. Liu, H. Wang, J.W. Xu, L. Yang, W. Qiu, S.J. Zhou, J. Electron. Mater. **51**, 831–837 (2021)

15. G.B. Hu, J.T. Wang, X. Liu, H.N. Liu, H. Wang, J.W. Xu, L. Yang, C.R. Zhou, W. Qiu, J. Mater. Sci. Mater. Electron. **32**, 22300–22308 (2021)

16. X. Wu, C.G. Fang, J.F. Lin, C.W. Liu, L.H. Luo, M. Lin, X.H. Zheng, C. Lin, Ceram. Int. **44**, 4908–4914 (2018)

17. X.M. Zhao, X.L. Chao, D. Wu, P.F. Liang, Z.P. Yang, J. Alloys Compd. **798**, 669–677 (2019)

18. Z.H. Dai, D.Y. Li, Z.J. Zhou, S. Zhou, W.G. Liu, J.J. Liu, X. Wang, X.B. Ren, Chem. Eng. J. **427**, 131959 (2022)

19. Q.Z. Chai, X.M. Zhao, X.L. Chao, Z.P. Yang, RSC Adv. **7**, 28428–28437 (2017)

20. X.S. Zhang, D. Yang, Z.Y. Yang, X.M. Zhao, Q.Z. Chai, X.L. Chao, L.L. Wei, Z.P. Yang, Ceram. Int. **42**, 17963–17971 (2016)

21. M. Kosec, V. Bobnar, M. Hrovat, J. Bernard, B. Malic, J. Holc, J. Mater. Res. **19**, 1849–1854 (2004)

22. Z.Y. Liu, H.Q. Fan, B.L. Peng, J. Mater. Sci. **50**, 7958–7966 (2015)

23. J. Fu, R.Z. Zuo, Y.D. Xu, J.F. Li, M. Shi, J. Eur. Ceram. Soc. **37**, 975–983 (2017)

24. C. Lin, X. Wu, M. Lin, Y.P. Huang, J. Li, J. Alloys Compd. **706**, 156–163 (2017)

25. Q.Z. Chai, D. Yang, X.M. Zhao, X.L. Chao, Z.P. Yang, J. Am. Ceram. Soc. **101**, 2321–2329 (2018)

26. H. Xie, G.B. Liu, L. Yang, S.J. Pang, C.L. Yuan, X.W. Zhang, H. Wang, C.R. Zhou, J.W. Xu, J. Mater. Sci. Mater. Electron. **29**, 19123–19129 (2018)

27. P.D. Gio, T.T. Bau, N.V. Hoai, N.Q. Nam, J. Mater. Sci. Chem. Eng. **08**, 1–11 (2020)

28. G.B. Hu, H.N. Liu, J.T. Wang, Y.B. Sun, H. Wang, J.W. Xu, L. Yang, C.R. Zhou, J. Electron. Mater. **50**, 968–977 (2020)

29. A. Rahman, S. Park, Y. Min, G.T. Hwang, J.J. Choi, B.D. Hahn, K.H. Cho, S. Nahm, C.W. Ahn, J. Eur. Ceram. Soc. **40**, 2989–2995 (2020)

30. B.Y. Qu, H.L. Du, Z.T. Yang, J. Mater. Chem. C **4**, 1795–1803 (2016)

31. L. Gao, W.C. Zhou, F. Luo, D.M. Zhu, J. Wang, Ceram. Int. **43**, 12731–12735 (2017)

32. K. Li, F.L. Li, Y. Wang, K.W. Kwok, H.L.W. Chan, Mater. Chem. Phys. **131**, 320–324 (2011)

33. X.M. Zhao, Q.Z. Chai, B. Chen, X.L. Chao, Z.P. Yang, J. Am. Ceram. Soc. **101**, 5127–5137 (2018)

34. Z.M. Geng, K. Li, D.L. Shi, L.L. Zhang, X.Y. Shi, J. Mater. Sci. Mater. Electron. **26**, 6769–6775 (2015)

35. J.P. Sharma, D. Kumar, A.K. Sharma, Solid State Commun. **334–335**, 114345 (2021)

36. J. Zhang, L. Yang, J.W. Xu, C.R. Zhou, C.L. Yuan, H. Wang, G.H. Rao, J. Alloys Compd. **881**, 160512 (2021)

37. Y.J. Zhao, Y.J. Dai, H.P. Zhou, X.W. Zhang, J. Alloys Compd. **731**, 39–43 (2018)

38. K. Nakano, K. Oka, T. Watanuki, M. Mizumaki, A. Machida, A. Agui, H. Kim, J. Komiyama, T. Mizokawa, T. Nishikubo, Y. Hattori, S. Ueda, Y. Sakai, M. Azuma, Chem. Mater. **28**, 6062–6067 (2016)

39. Y.Y. Li, P.X. Xiong, G.C. Liu, M.Y. Peng, Z.J. Ma, Inorg. Chem. **60**, 13510–13516 (2021)

40. Z. Wang, H.S. Gu, Y.M. Hu, K. Yang, M.Z. Hu, D. Zhou, J.G. Guan, CrystEngComm **12**(10), 3157–3162 (2010)

41. A.M. El Nahrawy, A.B. Abou Hammad, A.M. Mansour, Arab. J. Sci. Eng. **46**, 5893–5906 (2020)

42. A.M. El Nahrawy, A.M. Mansour, A.B. Abou Hammad, A.R. Wassel, Mater. Res. Express **6**, 016404 (2018)

43. J.F. Lin, Q.L. Lu, J. Xu, X. Wu, C. Lin, T.F. Lin, C. Chen, L.H. Luo, J. Am. Ceram. Soc. **102**, 4710–4720 (2019)

44. X.M. Zhao, X.L. Chao, D. Wu, P.F. Liang, Z.P. Yang, J. Am. Ceram. Soc. **102**, 3498–3509 (2018)

45. X. Liu, H.L. Du, X.C. Liu, J. Shi, H.Q. Fan, Ceram. Int. **42**, 17876–17879 (2016)

46. L. Cao, Y. Yuan, E.Z. Li, S.R. Zhang, Ceram. Int. **45**, 5660–5667 (2019)

47. L.X. Xie, J. Xing, Z. Tan, L.M. Jiang, Q. Chen, J.G. Wu, W. Zhang, D.Q. Xiao, J.G. Zhu, J. Alloys Compd. **758**, 14–24 (2018)